Elastic wave propagation in smooth and wrinkled stratified polymer films

OPEN ACCESS
IOP Publishing
Nanotechnology

Nanotechnology **30** (2019) 045709 (12pp)
https://doi.org/10.1088/1361-6528/aaee9b

Elastic wave propagation in smooth and wrinkled stratified polymer films

M Hesami[1], A Gueddida[2], N Gomopoulos[1], H S Dehsari[1], K Asadi[1], S Rudykh[3], H-J Butt[1], B Djafari-Rouhani[2,4] and G Fytas[1,4]

[1] Max Planck Institute for Polymer Research, Ackermannweg 10, D-55128, Mainz, Germany
[2] Institut d'Electronique, de Microélectronique et de Nanotechnologie (IEMN), UMR-CNRS 8520, Département de Physique, Université de Lille 1, F-59655, Villeneuve d'Ascq, France
[3] Department of Mechanical Engineering, University of Wisconsin—Madison, Madison, WI 53706, United States of America

Received 27 September 2018, revised 23 October 2018
Accepted for publication 6 November 2018
Published 28 November 2018

Abstract

Periodic materials with sub-micrometer characteristic length scale can provide means for control of propagation of hypersonic phonons. In addition to propagation stopbands for the acoustic phonons, distinct dispersive modes can reveal specific thermal and mechanical behavior under confinement. Here, we employ both experimental and theoretical methods to characterize the phonon dispersion relation (frequency versus wave vector). We employed Brillouin light scattering (BLS) spectroscopy to record the phonon dispersion in stratified multilayer polymer films. These films consist of 4–128 alternate polycarbonate (PC) and poly (methyl methacrylate) (PMMA) layers along and normal to the periodicity direction. The distinct direction-dependent phonon propagation was theoretically accounted for, by considering the polarization, frequency and intensity of the observed modes in the BLS spectra. Layer-guiding was also supported by the glass transition temperatures of the PC and PMMA layers. The number of phonon dispersion branches increased with the number of layers but only a few branches were observable by BLS. Introduction of an additional in-plane periodicity, through a permanent wrinkling of the smooth PC/PMMA films, had only subtle consequences in the phonon propagation. Using the frequencies of the periodicity induced modes and momentum conservation equation we were able to precisely back calculate the wrinkle periodicity. However, a wrinkling-induced acoustic stopband utilizing flexible layered materials is still a challenge.

Supplementary material for this article is available online

Keywords: phononics, dispersion diagram, elastodynamic simulation, wrinkled film, glass transition

(Some figures may appear in colour only in the online journal)

Introduction

Wave propagation in periodic materials has been intensely studied during the last decades [1, 2] due to its diverse application in different fields including photonic crystals [3], sound shields [4], acoustic diodes [5], vibration damper [6, 7] and thermal management [8, 9]. Understanding the wave propagation phenomenon in periodic structures allows one to control over the properties, and to design materials with tailored features. One-dimensional (1D) multi-layers are fundamental model systems to study the phonon propagation both along and normal to the periodicity direction [10–13]. By changing the elastic impedance contrast, phononic band gaps can be opened and the bandwidth can be tuned by changing the material characteristics [14, 15]. For low elastic

[4] Authors to whom any correspondence should be addressed.

contrast, phonon propagation is confined in 1D polymer based multilayers exemplifying infinite slabs, where air-interface effects are negligible [16]. Such interfacial impact on the phonon propagation can be addressed in finite number of layers, i.e. stratified oligo-layers.

The interfacial effect on phonon propagation of non-periodic structures has been studied for free standing and supported thin films with air interfaces only and substrate and air interfaces, respectively [17–19]. In the case of multilayer films, however, not only the air interface but also the layer-layer interface might affect the phonon propagation. One aim of this work is to address the interfacial impacts on phonon propagation in finite 1D oligo-layer of polycarbonate (PC)/poly methyl methacrylate (PMMA). We studied the phonon propagation parallel and normal to the layer plane using Brillouin light spectroscopy (BLS) and elastodynamic simulations. The nature of the propagated phonons was further examined by temperature scanning measurements and displacement field calculations.

In nature, many periodic structures have undulating and wrinkled patterns which can regulate optical properties [20] and save the insect's life [21]. In addition, wrinkled multilayer structures might also change their phononic behavior. Recently, it was theoretically shown that interfacial wrinkles, formed due to mechanical instability, in compressed layered structures can induce band gaps in elastic wave propagation [22]. While wrinkled multilayer composites in a millimeter scale were fabricated using 3D printing [23] their fabrication in the sub-micrometer scale is still a challenge. In the sub-micrometer scale, surface wrinkled structures or single wrinkled layers are usually prepared by buckling of a stiff thin layer supported on a compliant matrix [24–28]. Limited number of wrinkled layers can be fabricated layer by layer assembly [29] and nanotransfer printing [30]. In addition, conservation of the periodicity in the direction normal to the layers requires precise layer deposition to minimize phase change among subsequent layers. To overcome such problems, we proposed a novel method based on a nanoprinting on a consolidated flat 1D multilayer film. The pattern can be transferred through polymer layers with the same periodicity leading to a 2D wrinkled structure with two mutually orthogonal periodicities.

The quality of the fabricated wrinkled films (WFs) and the impact on the phonon propagation was investigated in PC/PMMA multilayer films with different layer periodicity, D, through BLS and elastodynamic simulations. The intensity of the first and second order optical harmonics due to the wrinkling periodicity, D', depend on the layer periodicity, D. However, the phonon dispersion in WFs is marginally modified, in contrast to the theoretical prediction of instability induced phononic band gap in compressed 1D structures [22, 31]. In the latter case, the modification of the dispersion curves results from a combined effect of the structure deformation and the high sensitivity of the elastic moduli to the applied external stimuli (stress, electric field), especially in the vicinity of the interfacial wrinkling instability. However, the wrinkling periodicity does not enter into the theoretical band diagram of these deformable structures. In the presence case, the introduction of the additional stationary periodicity in the wrinkled 1D structures is well represented by the theory without the necessity of making any change in the material parameters.

Experimental

PC/PMMA multilayer films with different film thickness and compositions were used. Oligo-layer of PC/PMMA films with a symmetric composition and layer thickness of 390 nm have 4, 8 and 16 layers were used, and finite effects were compared with PC/PMMA with 32 and 128 layers. The multilayer flat films were prepared by layer-multiplying co-extrusion [32, 33]. For fabrication of WFs, a structured polydimethylsiloxane (PDMS) stamp consisting of both hard and soft PDMS was employed. The PDMS stamps were prepared using a 4 inch 'silicon master' with anti-sticking coating (NIL Technology, Denmark). The PDMS stamps were prepared from Sylgard 184 silicone elastomer mixed with a curing agent (Dow Corning, USA) in a ratio of 10:1 by weight. After casting of the silicone elastomer mixture on to the master, the stamp/master assembly was placed in a desiccator to detrap air bubbles. Subsequently, to cure the stamp, the stamp/master assembly was heated up and kept at 60 °C, for 3 h. Finally, the PDMS stamp was peeled off the master.

The WF have constant total thickness (~50 μm). Three bilayer periodicities, D, 780 nm (WF128), 390 nm (WF256) and 195 nm (WF512) with 128, 256 and 512 layers were examined. The periodicity of the gratings, D', on the stamp was 600 and 700 nm while its depth was 500 nm. To create the wrinkled periodicity, the PDMS stamp was placed onto a flat multilayer film. The construction was first heated up to 413 K and then a pressure of 100 MPa was applied to the stamp as shown in figure 1(a). We tried different pressures and temperatures, and found that the optimum pressure and temperature are around 100 MPa and 413 K, respectively. The films were kept for 60 min at this condition. Finally, the pressure was released, and the film was rapidly cooled to the room temperature. It is assumed that above the glass transition temperature of the softer component (PMMA), this layer is soft enough and can act as an internal stamp for transforming the pattern through the stack thickness. To evaluate the efficiency of the stamping, the top surface and the microtomed cross section of the film were observed with scanning electron microscope (LEO Gemini 1530, Zeiss, Germany).

The diffracted pattern of the flat film, PDMS stamp and WF were compared after shining a 532 nm laser light. From figure 1(b) it can be seen that the diffracted pattern of the PDMS stamp and WF are similar, however, the flat film revealed only one bright point. The expected bright interference spots from the PMDS stamp with the grating patterns were also observed for the wrinkled confirming the pattern transformation to the flat film. However, in the WF, the spots are stretched due to the wavy structure of the transferred patterns as confirmed by the AFM image in the inset of figure 1(c). The SEM image of the top surface of the film, which was in contact with the stamp, confirms the formation of the wrinkles with a periodicity of about 800 nm. SEM

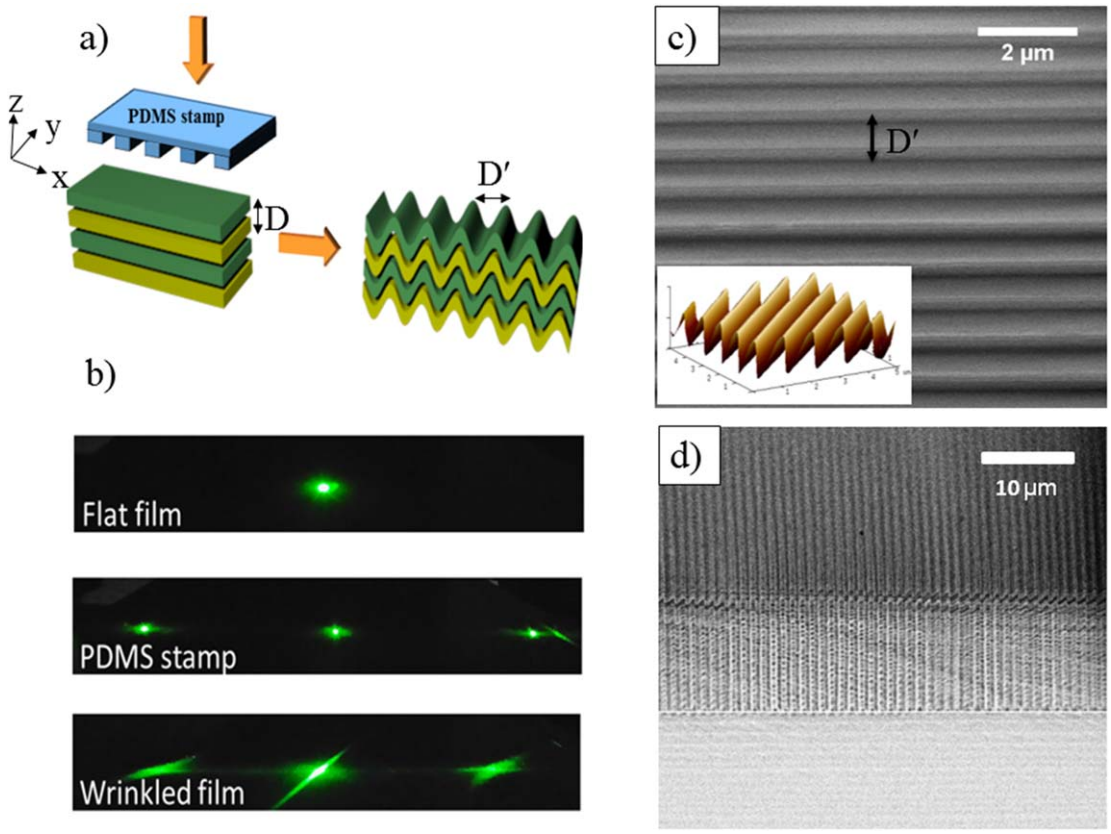

Figure 1. (a) Fabrication of winkled films (WF) from flat bilayer flat film (FF) consisting of 510 nm PMMA (yellow) and 270 nm PC (green) monolayers. (b) Diffraction of a 532 nm laser light from the PDMS stamp, the smooth PC/PMMA film with 128 layers and the corresponding wrinkled film. (c) SEM images of the top surface and (d) cross section of a wrinkled film with 128 layers.

imaging was also done on the cross section of the WF (figure 1(d)) after micro cutting (ultramicrotome EM UC7, Leica, Germany). Here, the vertical and the horizontal periodicities are due to the wrinkles and layer patterns, respectively. By measuring the width of the wrinkled part at three different lateral positions and dividing the average value by the total film thickness (50 μm), the wrinkling efficiency is observed to be around 50%.

BLS employed on transparent films is based on photoelastic interaction of an incident visible photon (532 nm) and a thermally excited phonon. This inelastic scattering results in a spectrum $I(\mathbf{q}, \omega)$ where $\mathbf{q} = \mathbf{k_s} - \mathbf{k_i}$ (here $\mathbf{k_s}$ and $\mathbf{k_i}$ are the wave vectors of the scattered light and incident laser beam) is the scattering wave vector and ω is the frequency shift of the scattered light. For a homogeneous medium, the probed phonon has $\mathbf{k} = \mathbf{q}$. For a periodic structure with a reciprocal lattice vector $\mathbf{G}$, momentum conservation requires $\mathbf{k} = \mathbf{q} \pm \mathbf{G}$. For different samples, the spectrum was recorded at different wave vectors and the dispersion relation is represented by the plot $\omega(k)$ along a propagation direction selected by the scattering geometry. In the present study, BLS was used in both the transmission and reflection scattering geometry (please see supporting information figure S1, which is available online at stacks.iop.org/NANO/30/045709/mmedia). In this case, the scattering wave vector $\mathbf{q}$ is parallel to the layers with magnitude $q_{//} = (4\pi/\lambda) \sin \alpha$ independent of the refractive indices of the layers, where $\lambda = 532$ nm. However for the reflection geometry the scattering wave vector is dependent on the refractive index which was kept constant to 1.5 [1]. Temperature-dependent measurements were performed by placing the sample into a heating chamber, and heating the sample up to the desired temperature by multiple steps. At each measuring temperature, the sample was equilibrated for about 15 min before recording the spectrum. Then BLS data were acquired for about 30 min for each scan. In the present study, BLS was used in both the transmission and reflection scattering geometry.

Theoretical calculations of the dispersion curves (frequency versus wave vector) of the films are obtained by solving the elasticity equations of motion in the heterogeneous material by using COMSOL Multiphysics software based on the finite element method (FEM). The governing equations of motion that describe the propagation of phonons in each constituting material are given by:

$$-\rho\omega^2 \boldsymbol{u} = \nabla \boldsymbol{\sigma} \tag{1}$$

ρ is the mass density, ω is the pulsation of phonon, $\boldsymbol{u}$ the displacement field and $\boldsymbol{\sigma}$ is the elastic stress tensor. The elastic field satisfies the boundary conditions at any interface between two different constituents, namely the continuity of the displacements and of the normal stresses. The proposed structure consisted of a finite number of layers along z direction and considered as infinite in both x and y directions,

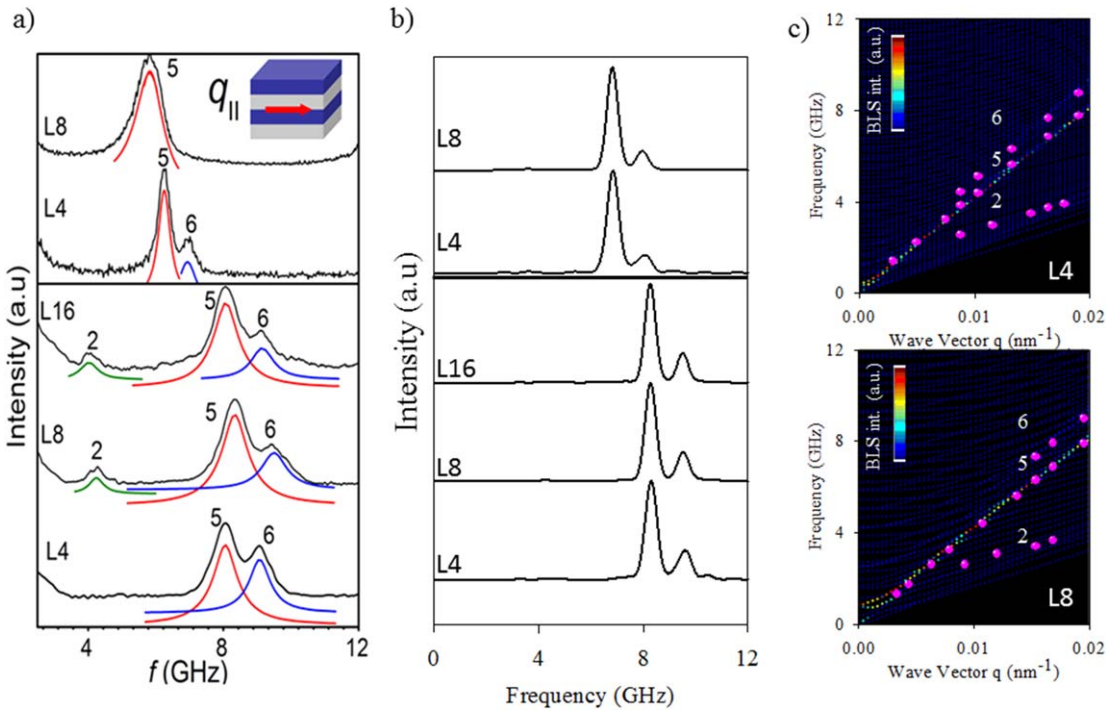

Figure 2. (a) Isotropic polarized (VV) BLS spectra for in plane propagation in PC/PMMA multilayer films with 4, 8 and 16 layers at $q_{II} = 0.0205\ \text{nm}^{-1}$ being directed parallel to the layers as schematically shown in the inset of the upper panel. The upper panel of figure 2(a) displays the BLS spectra of L4 and L8 at a lower $q_{II} = 0.0167\ \text{nm}^{-1}$. The solid lines on the anti-Stokes side of the spectrum denote the representation with Lorentzian lines convoluted with the instrumental function. (b) Theoretical spectra (convoluted with broadening of 0.2 GHz) for L4, L8 and L16 at $q_{II} = 0.0205\ \text{nm}^{-1}$ (lower panel) and for L4 and L8 at $q_{II} = 0.0167\ \text{nm}^{-1}$ (upper panel). (c) Theoretical and experimental (pink points) dispersions for L4 and L8.

with an additional periodicity along x in the case of wrinkled structures. In the latter case, Bloch theorem is applied for propagation along x, with the periodicity of the wrinkles. To obtain the phononic properties, free stress boundary conditions are applied at the top and bottom of the whole film. Under these considerations, the dispersion curves can be calculated for propagation along x or y directions and the obtained modes correspond to stationary waves in the thickness of the film (along z). When the number of layers in the film becomes infinite, we obtain a superlattice (SL) structure in which the Bloch theorem can also be applied for propagation along z.

Results

Wave propagation in polymer Bragg stacks. Finite effects

The air-surface impact on the phonon propagation can be addressed in finite number of stratified layers, i.e. oligo-layers. Figure 2(a) shows isotropic BLS spectra (anti-Stokes) recorded at 293 K for in-plane propagation in PC/PMMA oligo-layer films with 4, 8 and 16 layers at $q_{II} = 0.0205\ \text{nm}^{-1}$ (lower panel) and 4 and 8 layers at $q_{II} = 0.0167\ \text{nm}^{-1}$ (upper panel). The spectra displaying more than one mode were represented by Lorentzian line shapes (solid lines). Three distinct modes (2, 5, 6) have been resolved in the experimental BLS and their frequencies at the peak position were studied as a function of the wave vector, q_{II}; for comparison we keep the same codes of the modes as in [16]. According to the spectra of figure 2(a), the intensity of mode 6 depends both on q_{II} (L8 in upper and lower panel) and the number of layers (L4, L16 in the lower panel). Note that at $q_{II} = 0.0167\ \text{nm}^{-1}$, mode 6 is present in L4 but not discernible in L8 (upper panels in figures 2(a) and (b)).

From the analysis of the dispersion curves, one can derive the BLS spectra (frequency and intensity) based on the photo-elastic mechanism of photon-phonon interaction which is the main elasto-optic mechanism in transparent materials [14, 34]. We assume that the contribution of the interfacial motion to the scattering is small, since the constituting materials possess very similar refraction indices [14, 35, 36]. The interaction is based on the change in dielectric permittivity tensor $\delta\varepsilon_{ij}$ at each point of the sample due to its modulation by the acoustic wave according to the proportionality of $\delta\varepsilon_{ij}$ to the elastic strain S_{kl}, $\delta\varepsilon_{ij} = P_{ijkl}\, S_{kl}$ where P_{ijkl} is the photo-elastic tensor. In isotropic materials, there are only two independent photo-elastic coefficients, namely P_{11} (=P_{1111}) and $P_{12} = P_{13}$ (P_{1122}). A simple approach of the Brillouin intensity is then given by [37]:

$$I(\omega, q) = |E_j^S|^2 \propto \left| \frac{1}{\omega} \int\int_{unit.cell} e^{iqr} \sum_{ikl} P_{ijkl} S_{kl} E_i^I \, dS \right|^2, \quad (2)$$

where E_j^S is the j component of the scattered electric field, E_i^I is the i component of the electric field of the laser beam, q is the wave vector, P_{ijkl} are the components of the photoelastic tensor, and S_{kl} are the components of the strain tensor. In our

scattering geometry, we assume that the scattered electric field E^S and the incident electric field E^I are both polarized perpendicular to the sagittal plane defined by the direction of propagation (x or y or z) and the normal to the film (z axis). Then, in the general geometry of WFs, the above expression can be written explicitly, namely, for propagation along x direction,

$$I(\omega, q) \propto \left| \frac{1}{\omega}\int\int_{unit.cell} e^{iqx}\left(P_{12}^{\alpha}\left(\frac{\partial u_x}{\partial x}+\frac{\partial u_z}{\partial z}\right)\right) + P_{11}^{\alpha}\frac{\partial u_y}{\partial y}\right)E^0 dS \Bigg|^2. \quad (3)$$

When applied to the simpler case of flat films, the components (u_x, u_z) of the displacement field are decoupled from the component u_y and each part can be considered independently (here we consider only the former modes), thus, for propagation parallel to y direction (normal to the wrinkle periodicity):

$$I(\omega, q) \propto \left| \frac{1}{\omega}\int\int_{unit.cell} e^{iqy}\left(P_{11}^{\alpha}\frac{\partial u_x}{\partial x}+P_{12}^{\alpha} \times\left(\frac{\partial u_z}{\partial z}+\frac{\partial u_y}{\partial y}\right)\right)E^0 dS \Bigg|^2. \quad (4)$$

Finally, for propagation along z direction:

$$I(\omega, q) \propto \left| \frac{1}{\omega}\int\int_{unit.cell} e^{iqz}\left(P_{11}^{\alpha}\frac{\partial u_x}{\partial x}+P_{12}^{\alpha}\frac{\partial u_z}{\partial z}\right)E^0 dS \Bigg|^2. \quad (5)$$

When applied to the case of the flat films, the three components of the displacement field are decoupled from each other and we limit ourselves to longitudinal waves with the u_z component only. Figure 2(b) presents the theoretical calculations of the BLS spectra which correspond to the experimental spectra in figure 2(a) (for two values of the wave vector $q_{//} = 0.0167$ and $0.0205\ \mathrm{nm}^{-1}$) and different samples L4, L8 and L16. The theoretical spectra were convoluted by the instrumental function considering different widths (see figure S2). There are two peaks 5 and 6, the latter being relatively weaker than the former. Their frequencies appear to be robust over the variation of number of layers from L16 to L4, in agreement with the experimental trend in the lower panel of figure 2(a). The theory predicts similar spectral shape for both L4 and L8 at a lower $q_{//}$ ($=0.0167\ \mathrm{nm}^{-1}$ upper panel in figure 2(b)), whereas the experimental spectrum of L8 displays a broad single peak (upper panel of figure 2(a)). The weaker 6 mode is still present, however, it cannot be experimentally resolved due to the broad linewidths. At even lower $q_{//}$'s, only the strong mode 5 survives in agreement with the theoretical prediction (figure 2(c)).

The theoretical dispersion curves for L4 and L8 are presented in figure 2(c). The color scale represents the BLS intensity of the displayed modes. The experimental frequencies of modes 5 and 6 are indicated by pink points. Mode 5 is visible up to very low wave vectors, while the intensity of mode 6 vanishes at low $q_{//}$ ($<0.01\ \mathrm{nm}^{-1}$). This behavior may be related to the change in polarization of mode 6, when approaching low wave vector; namely, an increase in the transverse component of the displacement field with respect to its longitudinal component. The frequency of the main modes is in a good agreement with the predicted values of the theoretical dispersion in figure 2(c) for the L8 and L4 films. The bands with large BLS intensity are colored towards red, while those with zero intensity are shown in dark blue. We note the good agreement with the theoretical predictions without any need to adjust parameters. Mode 5 represents the main longitudinal mode in the considered q-region and, has the effective medium sound velocity $\sim 2600\ \mathrm{m\,s}^{-1}$ which falls between the longitudinal speed of sound in the PC ($c_1 = 2430\ \mathrm{m\,s}^{-1}$) and PMMA ($c_1 = 2850\ \mathrm{m\,s}^{-1}$) components. We note that this mode might deviate from the pure acoustic behavior due to its increasing localized nature with reducing number of layers according to the theoretical predictions (figures 2(c) and 3 below).

The nature of the two modes can further be elucidated through the comparison of the dispersion relation and displacement field of the bilayer L4 with an infinite number of layers (SL) shown in figure 3. The upper panel of figure 3(a) displays the dispersion curve of a SL (periodicity along z) for propagation parallel to the layers, i.e. $q_{//}$ parallel to x (hence $q_z = 0$); the dispersion diagram is not given for other values of q_z, because the periodicity along z imposes the condition $q_z = 0$. For L4 film, the dispersion relation is displayed in the lower panel of figure 3(b), also for in-plane phonon propagation. Owing to the finite thickness of L4 and therefore lack of periodicity along z, a choice for q_z is not possible. Therefore, the modes are selected so that they are stationary inside the film thickness, and they satisfy the free-stress boundary conditions at the top and bottom interfaces being in contact with air. For a given $q_{//}$ (parallel to x), the boundary conditions define the values of q_z in the range from 0 to π/D. Therefore, the dispersion curves can be interpreted as guided modes in the finite L4 film. The number of dispersion curves increases for the thicker L8 and in the limit of a SL (infinite number of layers), the number of branches becomes infinite. However, the selection rule about the choice of q_z becomes more efficient with increasing number of layers in the film and in the limit of infinite SL only the $q_z = 0$ modes are active as presented in the upper panel of figure 3(a).

Comparison of the dispersion diagram of SL and the present oligo-layers reveals that a SL film displays an effective medium behavior in the low q region, while the oligo-layers exhibit Lamb modes. This is due to the fact that, for long phonon wavelength (at low $q_{//}$'s), the oligo-layers exhibit finite thickness plate-like behavior and, thus, the associated branches are similar to the Lamb modes [38] (see also figure 2(c)). From the many dispersive modes (finite frequencies at $q_{//} = 0$) corresponding to guided modes along x, only mode 6 was resolved (figure 2(a)). The BLS intensity of the higher branches is low due to a decreasing longitudinal component. The color scale in figure 3(a) presents the polarization of the branches (from red for longitudinal to blue for transverse). Intense BLS activity originates from longitudinal modes. For this reason, even the first guided branch

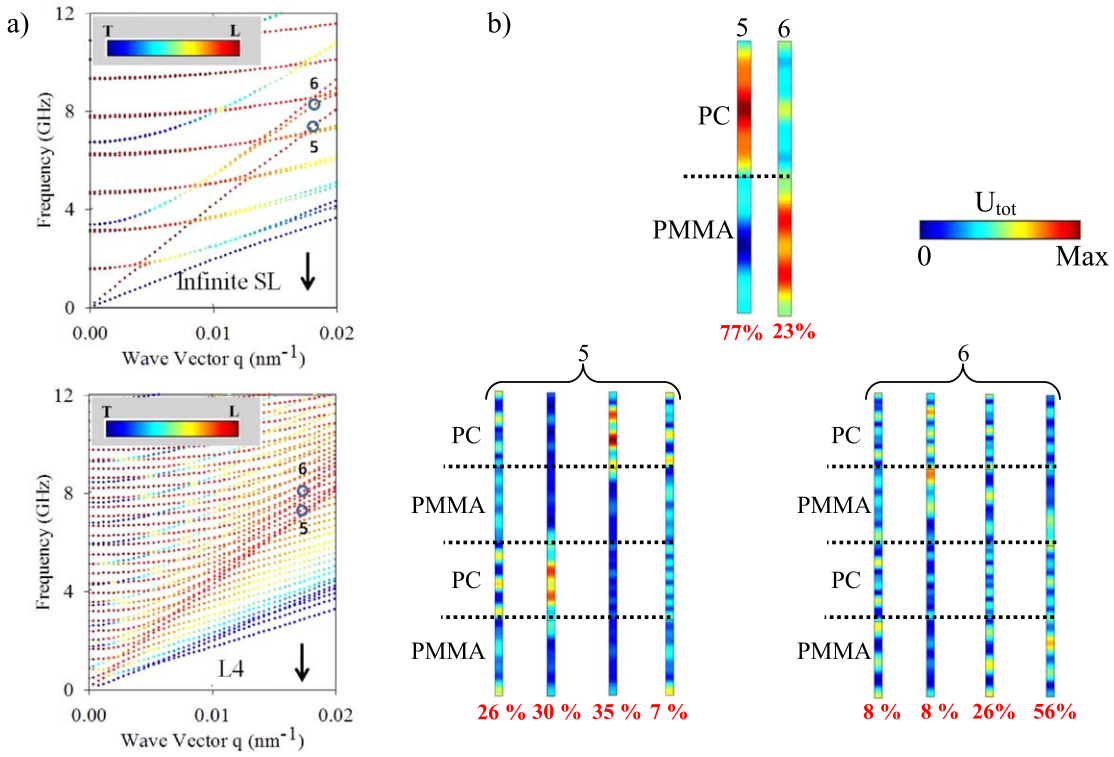

Figure 3. (a) Theoretical dispersion relation for super lattice (SL) (infinite number of layers, upper) and L4 (bottom) with color scale indicating the mixed transverse (*T*) and longitudinal (*L*) character. (b) Modulus of the displacement field calculated at $q_{//} = 0.0205\ \text{nm}^{-1}$ for modes indicated by circles on the dispersion diagram in (a). The percentages on the bottom of the field maps correspond to the contribution of the modes to the particular BLS peaks.

(represented by mode 6) becomes discernible at high—and not at low—$q_{//}$'s. For the SL, the polarization of mode 5 is longitudinal irrespectively of the number of layers, whereas the polarization of mode 6 changes from longitudinal to transverse with decreasing $q_{//}$ (figure 3(a)). Hence, mode 6 can be resolved only at high $q_{//}$'s in the BLS spectra of 128 L.

The localization of modes 5 and 6 depends on the number of layers. Figure 3(b), displays the displacement field of modes 5 and 6 at $q_{//} = 0.0205\ \text{nm}^{-1}$ for L4 and SL. In the upper panel of figure 3(b), we present the amplitude ($|u|$) of displacement fields of SL for modes 5 and 6, highlighted by a circle in figure 3(a). The intensity of mode 5 (77%) is almost three times higher than the intensity of mode 6 (23%) and is mostly localized in PC, whereas mode 6 belongs to the PMMA layers. There is no strict localization but predominance in PC or PMMA due to their rather lower elastic contrast. For the oligo-layer L4 film, the lower panel of figure 3(b) shows that each of the experimental peaks 5 and 6 is constituted by several modes. Their different contributions are indicated by the percentage at the bottom of these modes. As already mentioned, in thin films such as L4, there is no distinct q_z value, so there are a few modes contributing to the BLS peak in contrast to the SL.

To gain a deeper insight into the BLS intensities of the modes contributing to peaks 5 and 6 in L4 (figure 3(b)), we have calculated the complex scattering amplitudes for each layer in the film. For the modes contributing to peak 5, the displacement fields have a predominant confinement in the PC than in the PMMA layers, which also contribute predominantly to the scattering amplitudes. However, the contributions of both PC and PMMA layers interfere constructively and give rise to a relative high intensity of peak 5. For the modes contributing to peak 6, the displacement fields do not exhibit a clear confinement in the PMMA layers but rather spread over both types of layers. We note, however, that changing the relative thicknesses can modify the interference of the displacement fields, in particular, for weak field confinement, as in the present case.

Next, we examine the wave propagation normal to the layers utilizing the reflection geometry in the BLS setup (figure S1). Figures 4(a) and (b) refers to the experimental (a) and computed (b) BLS spectra at $q_{\perp} = 0.029\ \text{nm}^{-1}$ for PC/PMMA films with different number of layers at 293 K. The computed spectra represent theoretical spectra convoluted by the instrumental function using different broadening widths (figure S3). Figure 4(c) presents the displacement fields of the main modes contributing to the BLS spectra of L8 film at $q_{\perp} = 0.029\ \text{nm}^{-1}$; the corresponding plot for L4 is presented in figure S4. The number of the resolved peaks in the BLS spectra depends on the number of layers (figure 4(a)). For L128, the spectrum is unimodal and the main peak at 12.1 GHz corresponds to the longitudinal acoustic phonon propagating normal to the film plane. However, with decreasing number of layers this peak broadens and splits into a set of modes in L8 and L4. The splitting is clearer in the computed spectra (figure 4(b)). The computed spectra match their experimental counterparts. Owing to the high frequency range under consideration, the resolved modes (a), (b), (c)

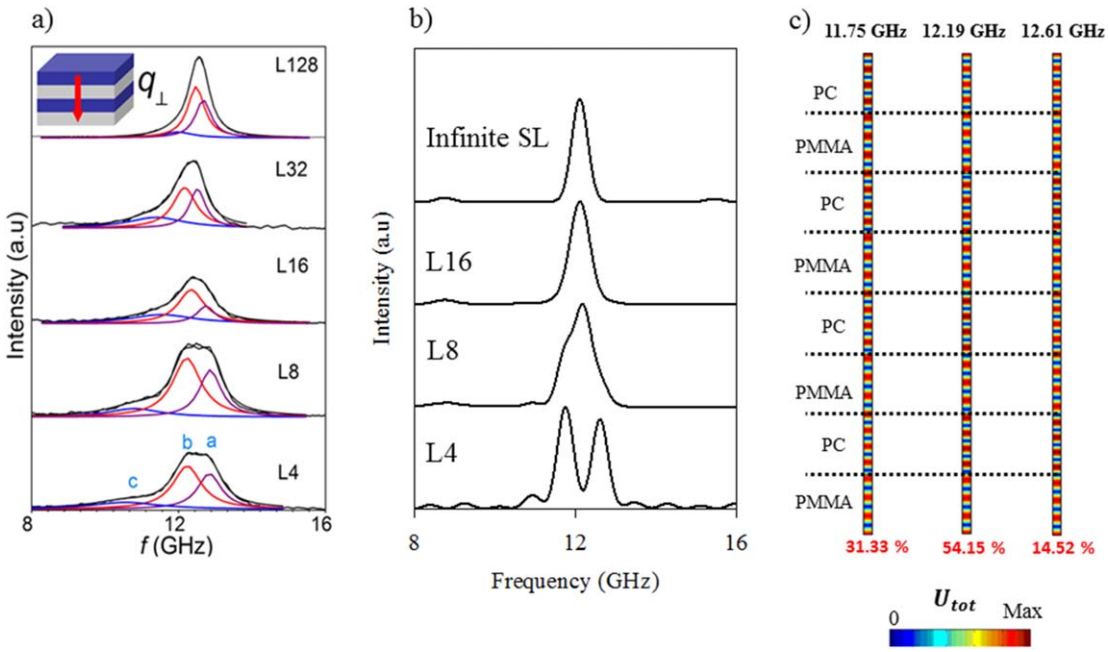

Figure 4. (a) Isotropic anti-Stokes BLS spectra for out-of-plane propagation in PC/PMMA multilayer films with different number of layers at $q_{\perp} = 0.029\ \mathrm{nm}^{-1}$. (b) Computed (convoluted with broadening of 0.2 GHz) BLS spectra at $q_{\perp} = 0.029\ \mathrm{nm}^{-1}$. (c) Modulus of the displacement field for the out-of-plane propagation in L8 calculated at $q_{\perp} = 0.29\ \mathrm{nm}^{-1}$, the contribution of the modes is indicated on the bottom of the field maps.

display numerous oscillations, due to short phonon wavelengths, in each layer of the bilayer structure. Therefore, the BLS intensities result from a complex interference phenomenon between the fields associated to the incident and scattered light and the involved phononic mode. For example, the modes in L8 have similar weights in the PC and PMMA layers. Also, the contributions from the constituent layers to the BLS amplitude are similar. The BLS amplitudes in PC and PMMA layers interfere constructively for each of the modes contributing to the peaks ((a)–(c)) of the L4 spectrum (figure S4). There are two main modes b and a, respectively at 11.75 and 12.6 GHz with similar relative weights, while the third mode at 10.93 GHz is much smaller. In L8 (figure 4(c)), the latter mode remains also very weak and there are three main contributing modes with the following frequencies and relative weights: 11.75 GHz (31.3%); 12.1 GHz (54.1%) and 12.6 GHz (14.5%), so the BLS spectrum contains a central peak surrounded by two shoulders.

In contrast to the displacement fields parallel to the layers (figure 3(b)), there is no preferred localization in any layer when propagation is normal to the layers. In this latter case, the displacement contribution is similar in different phases (PC or PMMA). It turns out that for low number of layers, the air interfaces (free surfaces) act as nodes. Due to multiple reflection of the acoustic excitation from the polymer and air interface, standing waves propagate in the material. We note that due to the relatively low elastic mismatch between the multilayer components, the polymer–polymer interface has not been sensed by the waves and they propagate with essentially the same contribution in different phases (as if in a homogenous material). The mode broadening [39] and splitting of the main peak [18] has been previously studied in supported thin films. In such cases due to large impedance contrast between the substrate and film, standing waves were observed. In our case, the film is free standing and the elastic impedance contrast, $\Delta Z = \frac{Z_{PC}}{Z_{air}} - 1$, between air and PC phase is sufficiently high ($\approx$7400) for standing waves to form [40].

To further examine the mode localization in oligo-layers and evaluate the effect of the interfaces (polymer–air and polymer–polymer) on the glass transition temperature (T_g) of the films, we varied the temperature at a constant q ($q_{ll} = 0.0205\ \mathrm{nm}^{-1}$, $q_{\perp} = 0.029\ \mathrm{nm}^{-1}$) for L4 and L8. The resulted softening temperatures were compared to the T_g of the individual components with different T_g's. The observed kink in the temperature dependence of the mode frequencies occurs at the temperature T_s ($\approx T_g$) at which the particular mode undergoes an abrupt softening due to glass–rubber transition of polymers [16, 41–44]. In figure 5, the shadowed bars highlight the softening regions (T_s) and the width of the bar stands for an error of ± 5 K. T_s is identified with the temperature at which an intersection between the two least-square-fitted straight lines occurs, due to abrupt changes in the volumetric and cohesive forces at the glass transition temperature [45].

Figures 5(a) and (b) demonstrate the results of temperature scanning for in-plane propagation, while the out-of-plane results are shown in figures 5(c) and (d). For mode 6 in L4 and L8, the observed $T_s \sim 375$ K corresponds to the $T_{g,PMMA}$ of PMMA. As soon as the temperature reaches the $T_{g,PMMA,}$ the sound velocity of the mode with field displacements in the PMMA (lower panel of figure 3(b)) senses the softening in the PMMA sublayer leading to the observed change of the decrease rate of the frequency at $T \sim T_{g,PMMA.}$ The effect is more obvious in the case of mode 6 (in-plane propagation) due to its sufficient localization as

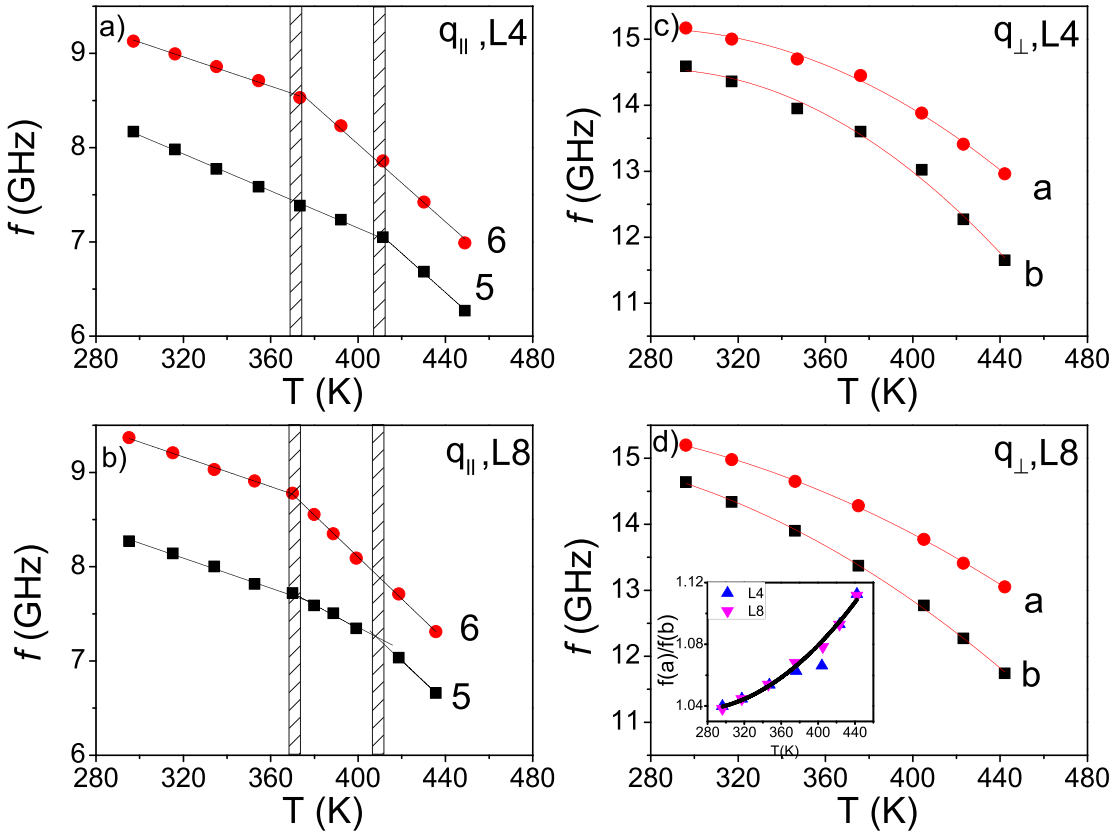

Figure 5. The softening transition temperatures (vertical shaded regions) for the in plane modes (5 and 6) at $q_{ll} = 0.0205\ \mathrm{nm}^{-1}$ (a) and (b) and for out-of-plane modes (a), (b) at $q_{\perp} = 0.029\ \mathrm{nm}^{-1}$ (c) and (d) in two oligo-layer films, L4 (a), (c) and L8 (b), (d). Solid lines in (a) and (b) represent linear fits of the experimental points before and after the transition. The experimental point in (c) and (d) were fitted using parabolic equation. Inset: the frequency ratio of modes (a) and (b) in out-of-plane propagation for L4 and L8.

reflected in the displacement field plot (figure 3(b)). For both L4 and L8, the slope dlnf(6)/dT assumes the value of 6.8×10^{-4} K which is typical for amorphous glassy polymers [44]. Above $T_{g,PMMA}$, the value of dlnf(6)/d$T = 1.3 \times 10^{-3}$ K^{-1} is again a typical value in the rubbery state [43, 44]. Even if mode 6 partially propagates though PC layers, the softening of this layer cannot be sensed due to the large slope already attained above $T_{g,PMMA}$. Instead it is mode 5, that undergoes the characteristic kink at $T \sim T_{g,PC}$ (=410 K) due to its stronger localization in the PC according to the displacement field contour plot (lower part of figure 3(c)). Below the glass transition of PC layer ($T_{g,PC}$), the slope dlnf(5)/dT =8.2×10^{-4} K^{-1} is surprisingly steeper (about 20%) than in the glassy PMMA rendering the resolution of $T_{g,PMMA}$ ambiguous. A possible account of this large (in glass) slope might indicate a leakage of mode 5 to PMMA layers or softening of the PMMA/PC interfaces.

For out-of-plane propagation, both modes a and b are standing waves with frequencies $f_m = 2m\,c_{\perp}/4$d, as the surfaces of the film (thickness d) are free of stress. The sound velocity $c_{\perp}$ is defined for homogeneous film. Still this value can approximate the effective medium sound velocity $c_{\perp}$ in the present case, since both materials (PMMA, PC) have comparable velocities. The temperature dependence of the frequency of the two modes is represented by a parabolic line with no discernible kink in contrast to the frequencies in figures 5(a) and (b). The glass–rubber transition in both layers is smeared out due to the concurrent decrease of $c_{\perp}$ with temperature and the change of the order m caused by thickness expansion. In fact, frequency ratio of the two modes is not robust to the temperature increase as shown in the inset of figure 5(d). Nevertheless, the distinct in-plane and out-of-plane propagation is manifested in the temperature dependence of the probed modes

Wave propagation in wrinkled polymer Bragg stacks

Periodic wrinkling of multilayer films with lattice constant, D, introduces a second periodicity, D', and renders the in-plane (x, y) propagation in WF direction dependent. In contrast to the smooth (flat) multilayers (FF) with the same number of layers [16], the phonon propagation along x (parallel to D') and along y (perpendicular to D') in WF (figure 1(a)) are distinct. This is shown in figure 6 for the in-plane band diagram of the WF128 (a), (b) and WF256 (d), (e) along the x (a), (d) and y (b), (e) and the corresponding smooth SL (c), (f) (in the plane x, y). For propagation along x, the wrinkled structure displays a periodicity along x with the first Brillouin zone (BZ) at π/D' (=0.0039 nm^{-1}). Thus, the band structure is presented in n-successive BZ along x, while $q_y = 0$ and $q_z = 2\mathrm{m}\pi/D$ (the periodicity of the FF film along z). For propagation along y, the band diagram of the WF structure displays a higher number of dispersion curves as compared to the FF film. Indeed for the band diagram of the smooth SL in figures 6(c), (f) the propagation wave vector is along y while

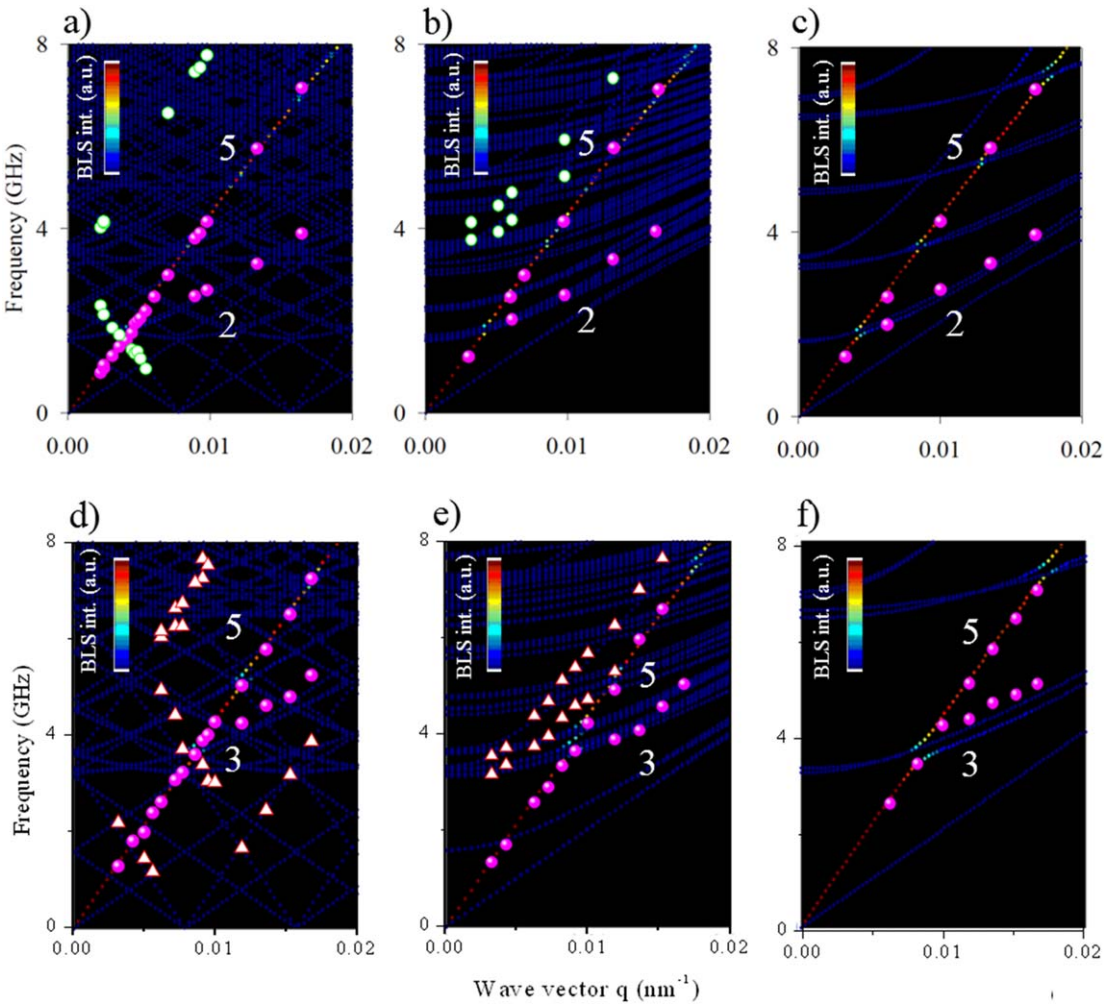

Figure 6. Theoretical band diagram for in-plane propagation in wrinkled 128 (a)–(c) and 256 (d)–(f) layered PC/PMMA film along (a), (d) and perpendicular (b), (e) to the wrinkle periodicity and in the corresponding smooth multilayer films (x, y plane in (c) and (f)). The solid pink symbols denote the experimental frequencies for the transverse mode 2 and longitudinal mode 5. The white solid symbols in (a), (d) and (b), (e) show the folded (periodicity induced) modes ($m = -1$, -2 and 1) (see figure 7(c)).

$q_x = 0$, while the band diagram of the WF film as a function of q_y in figures 6(b) and (e) contains the additional branches for which q_x can take the values $q_x = 2m\pi/D'$. Otherwise, the general trend and semi-quantitative behaviors for the WF film in figures 6(b) and (e) are the same as in the case of the smooth SL.

Figure 7 depicts in-plane BLS spectra of the WF128 containing 128 layers with $q_{//}$ being either along x (in figure 7(a)) or along y (in figure 7(b)), as schematically shown in the corresponding insets. The BLS spectra for WF256 are shown in figure S5(b). The modes (2, 5) appear in both WF and smooth SL. Compared to the theoretical band diagrams of figure 6, only few branches contribute to the spectra for both propagations along x and y. The frequencies of the observed experimental branches for both (q_x, q_y) phonon propagation are projected on the theoretical band diagrams of WF128 and WF256 in figure 6. Theory and experiments agreed for the two resolved modes in the BLS spectra and for both WF128 and WF256 samples. Notice that mode 2 in the spectra of WF128 sample has shifted to mode 3 in the WF256 samples.

For smooth films, the layer guided modes 2 and 3 are similar to their wrinkled counterparts. These modes are considered as layer eigen vibrations and their frequency at very small wave vectors ($q \to 0$) can be approximated with $f \sim c/D$ where c and D are the effective sound velocity and layer periodicity respectively. In the case of modes 2 and 3, c is the effective transverse sound velocity, $c_t = 1250\,\mathrm{m\,s^{-1}}$, because of the polarization of these modes when the wave vector approaches zero. The transverse velocity c_t can be deduced from the slope of the acoustic mode 1 in figure S5(d). By decreasing the layer periodicity (WF128 to WF256), the transverse layer guided mode 3 shifts to higher frequency with respect to mode 2. Therefore, for FF and WF512 samples, which have even a smaller periodicity along z, this mode could not be captured experimentally. Note that the layer mode 6, present in oligo-layer films (figure 2), decreases in intensity, when the number of layers is increased, and it becomes indiscernible in the multilayer films.

By comparing the spectra of WF128 (figures 7(a) and (b)) and WF256 and WF512 ($D = 195\,\mathrm{nm}$) with its smooth counterpart SL (figures S5(a)–(c)), one can conclude that some

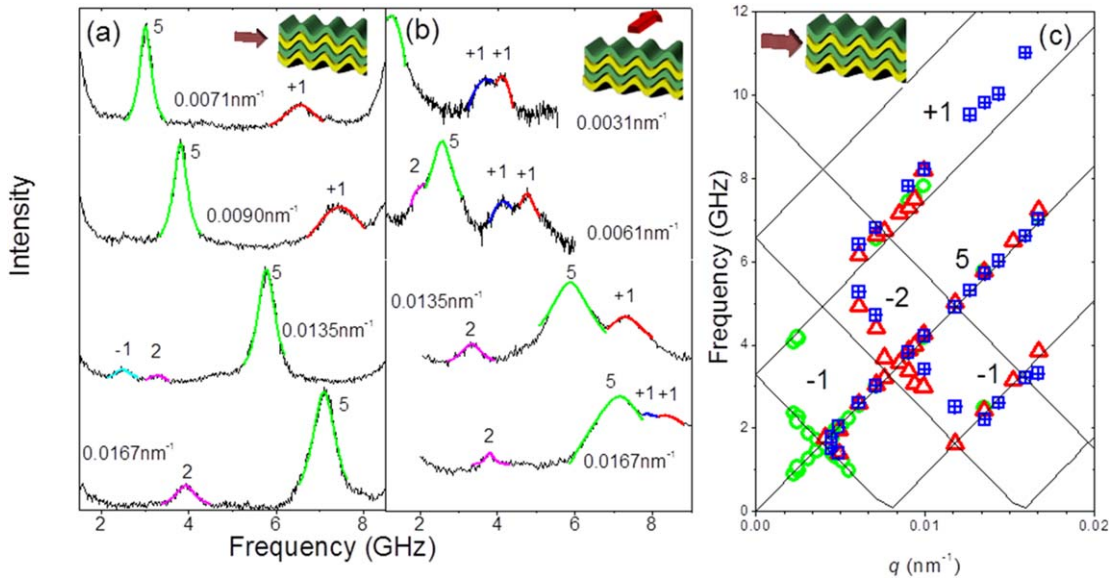

Figure 7. Typical isotropic (VV) BLS spectra of wrinkled WF128 film (a) along and (b) normal to the wrinkle periodicity (the red arrows in the inset show the $q_{//}$ parallel to layers). The solid lines on the anti-Stokes side of the spectrum denote the Lorentzian lines. Four modes are observed: (5), longitudinal acoustic, (+1), (−1) wrinkled induced periodicity modes and (2), transverse layer guided mode. (c) Dispersion diagram of WF samples, WF128: green, WF256: red and WF512: blue. The solid lines denote the representation of (−1), (−2) and (+1) by equation (6) using $c_{\text{eff}} = 2625\ \text{m s}^{-1}$ obtained from the mode 5 (solid line) and $D' = 800$ nm.

additional modes appear regardless of the relative orientation of $q_{//}$ to wrinkle periodicity. These modes are denoted with an integer n (1, 2) and '+' or '−' signs to indicate their relation to the periodicity. The VV spectra of WFs with three different layer periodicities D at different BZ are compared with the BLS spectra of their corresponding FF at the same wave vector q_x in figures S5(a)–(c). The denoted $\pm n$ modes arise from the optical diffraction caused by the wrinkles [38]. Since the films are wrinkled, they act as gratings that diffract the incident laser leading to additional phonons. Their frequencies (figure 7(c)), can be captured by momentum conservation (equation (6)), where $G = 2\pi m/D'$ *is* the reciprocal lattice constant, m is an integer …−2, −1, 0, 1, 2… defining the folded (or periodicity induced) modes and α is the relative angle between the probing wave vector $\boldsymbol{q}$ and the wrinkle periodicity D'. The c_{eff} was $2625\ \text{m s}^{-1}$, obtained from the longitudinal mode 5. The folded modes are also shown in figure 6 (white symbols) for the WF128 and WF256 films. The doublet appearance of $m = +1$ mode at low q's in figures 6(b), (e) is due to small deviations from $\alpha = 90^{\text{o}}$ in equation (6) (lifting of degeneracy).

$$f(k) = \frac{C_{eff}}{2\pi}\sqrt{G^2 + q^2 \pm 2G.q.\cos\alpha} \qquad (6)$$

The calculated frequencies of the periodicity induced modes according to equation (6) are shown as the solid lines in figure 7(c), and these results agree well with the experimental points, except for higher orders of harmonics or higher q's. For instance, mode −2 in whole q range and mode +1 at high q's deviate from the calculated values. Furthermore, we could not find mode −2 for WF128, which means that layer periodicity influences the optical harmonics and for largest periodicity (WF128, 780 nm) high order harmonics are not discernible. The intensity of the periodicity induced modes is highly dependent on the layer periodicity and quality of WFs (figure S6(b)). As it can be seen in figure S6(b), by decreasing the layer periodicity, mode '+1' becomes stronger in WF512 even stronger than the acoustic mode. Similarly, mode '−1' is weak for WF128 while it is stronger than acoustic for WF256 in figure S6(c). The periodicity induced modes can also be captured through layer periodicity. For smooth film, the out-of-plane measurements confirmed observation of mode −1 for smooth FF128 and FF256 films as shown in figure S7.

Based on the given explanation for the WFs, the band structure depends on the wrinkling and orientation of the wave vector. However, only a few branches are discernible in BLS, and they correspond to modes, which have similar characters in both wrinkled and flat films. Even in the theoretical band structure, the wrinkling does not give rise to opening of band gaps. This is partly due to the proximity of the elastic parameters in the constituting materials of our samples. However, even in calculations with a slightly higher contrast between the parameters, the band structure does not exhibit broad or complete band gaps resulting from the wrinkling. From this point of view, the theoretical work on instability-induced phononic band gaps in compressed 1D structures [22, 31] has a different framework than our seemingly similar 1D wrinkled SLs. In the former, the constituent materials obey a nonlinear constitutive law resulting in variation of the mechanical moduli with deformation. Moreover, these laminates—while remaining stable and flat—exhibit significant changes in their dispersion curves in the region near to the onset of microscopic instabilities (please see SI, for neo-Hookean laminates). Laminates under tension do not experience instabilities and remain flat, thus, the contribution of the material and geometrical changes can be evaluated directly; in such systems, the band gaps exist for elastic waves propagating in the direction *perpendicular* to the layers only. Considering the periodic system under mechanical

loading [46] or under the action of electric field [31, 47], it has been shown that the material and geometrical changes cancel each other for neo-Hookean laminates; whereas in materials exhibiting strong stiffening with deformation, such as Gent materials [46, 47], band gaps can be tuned by deformation. For laminates under exceeding compressive strain, it is not clear to what extent the opening of the phononic gap during strain relates to the change in the geometrical structure or to the change in the underlying material parameters. Based on a recent paper [31], while both changes contribute to the evolution of the band structure upon application of an external electric field, the modulation of the material properties plays a dominant role. In this case, strong modification of the dispersion curves can result from a combined effect of the structure deformation and the high sensitivity of the elastic moduli to the applied external stimuli (stress, electric field), especially in the vicinity of the interfacial wrinkling instability. In contrast to these theoretical investigations of nonlinear materials, for the present system the dispersion diagrams are well represented by the theory with the fixed material parameters that are not modified by deformation nor action of external fields. While the usage of hyperelastic models (such as neo-Hookean) proved to be useful in modeling of soft materials at macro- and micro-length scales, its applicability for smaller length-scales may be limited and the accuracy needs to be carefully verified. Small characteristic size of microstructure translate to higher frequency response, where rate dependent behavior is not significant, this is in contrast to the typical rate dependent behavior in soft composites at low frequencies [for soft composites with larger characteristic length of their microstructure.

Conclusions

We have studied the direction dependent propagation of high frequency phonons in multilayer polymer films consisting of 4–128 alternate PC and PMMA layers with periodicity in the sub-micrometer range. We utilized BLS to record the phononic dispersion curves along and normal to the periodicity direction. Theoretical calculations, obtained by solving the elasticity equations of motion in the nanocomposite material by using the FEM, allowed the assignment of the resolved branches in the experimental dispersion curves along the two propagation directions. For the in-plane phonon propagation (q in x, y plane) in PC/PMMA oligo-layers (4–16 layers), the three resolved modes (2, 5 and 6 with increasing frequency) relate to layer-guided Lamb modes with longitudinal (5) and transverse (2) polarizations, while mode 6 changes from longitudinal to transverse with decreasing q. The localization of modes 5 and 6 depends on the number of layers, and it is more pronounced in the multilayer films. The layer thickness was found to impact both the intensity and nature of modes 5 and 6. The layer-guided mode (6) loses amplitude above about ten layers due to interference of the displacement fields, whereas mode 5 transforms to the effective medium longitudinal phonon in the multilayer (128 256 layers) films.

The out-of-plane (q along z) propagation becomes distinct in the PC/PMMA oligo-layers in which the longitudinal acoustic phonon normal to the multilayer films transforms into standing waves with no preferred localization in any sublayer (PC or PMMA). Three such orders (a)–(c) modes were observed with increasing resolution from 32 to 4 layers as the air interfaces act as nodes enabling multiple reflections of the acoustic excitations. Due to the relatively low elastic mismatch between PC and PMMA, only the thickness of the oligo-layer film matters and the waves cannot sense the polymer–polymer interfaces. Apart of the theoretical account, an independent evidence of the resolved modes in the oligo-layers along both propagation directions stemmed from the temperature dependent study of their frequencies. The preferred localization of modes 5 and 6 to PC and PMMA was confirmed by the resemblance of two softening temperatures, respectively, to PC and PMMA glass transition temperatures.

Wrinkling implemented in the flat PC/PMMA multilayers by a nano printing technique introduced a second in-plane periodicity and lifted the direction invariance for the phonon propagation in the x, y plane. This permanent wrinkling of the smooth PC/PMMA films had only subtle consequences in the phonon propagation, apart from a strong photonic effect revealing the folded branches associated with the new periodicity. The latter allowed for a precise determination of the wrinkle periodicity knowing the effective acoustic velocity. High frequency and hence short wavelength acoustic wave propagation can provide detailed information on the material vibrations at nanoscale.

Acknowledgments

The work was supported by ERC AdG SmartPhon (No. 694977). SR thanks Dr Slesarenko for his help and discussions.

ORCID iDs

M Hesami https://orcid.org/0000-0002-3122-0108

References

[1] Alonso-Redondo E, Schmitt M, Urbach Z, Hui C, Sainidou R, Rembert P, Matyjaszewski K, Bockstaller M and Fytas G 2015 A new class of tunable hypersonic phononic crystals based on polymer-tethered colloids *Nat. Commun.* **6** 8309

[2] Alonso-Redondo E, Gueddida A, Huesmann H, El Abouti O, Tremel W, El Boudouti E, Djafari-Rouhani B and Fytas G 2017 Direction-dependent elastic properties and phononic behavior of PMMA/$BaTiO_3$ nanocomposite thin films *J. Chem. Phys.* **146** 203325

[3] Kang Y, Walish J J, Gorishnyy T and Thomas E L 2007 Broad-wavelength-range chemically tunable block-copolymer photonic gels *Nat. Mater.* **6** 957

[4] Gorishnyy T, Maldovan M, Ullal C and Thomas E 2005 Sound ideas *Phys. World* **18** 24

[5] Liang B, Guo X, Tu J, Zhang D and Cheng J 2010 An acoustic rectifier *Nat. Mater.* **9** 989

[6] Javid F, Wang P, Shanian A and Bertoldi K 2016 Architected materials with ultra-low porosity for vibration control *Adv. Mater.* **28** 5943–8

[7] Matlack K H, Bauhofer A, Krödel S, Palermo A and Daraio C 2016 Composite 3D-printed metastructures for low-frequency and broadband vibration absorption *Proc. Natl Acad. Sci.* **113** 8386–90

[8] Narayana S and Sato Y 2012 Heat flux manipulation with engineered thermal materials *Phys. Rev. Lett.* **108** 214303

[9] Davis B L and Hussein M I 2014 Nanophononic metamaterial: thermal conductivity reduction by local resonance *Phys. Rev. Lett.* **112** 055505

[10] Walker P, Sharp J, Akimov A and Kent A 2010 Coherent elastic waves in a one-dimensional polymer hypersonic crystal *Appl. Phys. Lett.* **97** 073106

[11] Saini G, Pezeril T, Torchinsky D, Yoon J, Kooi S, Thomas E and Nelson K 2007 Pulsed laser characterization of multicomponent polymer acoustic and mechanical properties in the sub-GHz regime *J. Mater. Res.* **22** 719–23

[12] Weber M F, Stover C A, Gilbert L R, Nevitt T J and Ouderkirk A J 2000 Giant birefringent optics in multilayer polymer mirrors *Science* **287** 2451–6

[13] Cheng W, Gorishnyy T, Krikorian V, Fytas G and Thomas E 2006 In-plane elastic excitations in 1D polymeric photonic structures *Macromolecules* **39** 9614–20

[14] Schneider D, Liaqat F, El Boudouti E H, El Hassouani Y, Djafari-Rouhani B, Tremel W, Butt H-J R and Fytas G 2012 Engineering the hypersonic phononic band gap of hybrid Bragg stacks *Nano Lett.* **12** 3101–8

[15] Döring F, Ulrichs H, Pagel S, Müller M, Mansurova M, Müller M, Eberl C, Erichsen T, Huebner D and Vana P 2016 Confinement of phonon propagation in laser deposited tungsten/polycarbonate multilayers *New J. Phys.* **18** 092002

[16] Cheng W, Gomopoulos N, Fytas G, Gorishnyy T, Walish J, Thomas E, Hiltner A and Baer E 2008 Phonon dispersion and nanomechanical properties of periodic 1D multilayer polymer films *Nano Lett.* **8** 1423–8

[17] Forrest J, Dalnoki-Veress K and Dutcher J 1997 Interface and chain confinement effects on the glass transition temperature of thin polymer films *Phys. Rev.* E **56** 5705

[18] Gomopoulos N, Cheng W, Efremov M, Nealey P and Fytas G 2009 Out-of-plane longitudinal elastic modulus of supported polymer thin films *Macromolecules* **42** 7164–7

[19] Cheng W, Sainidou R, Burgardt P, Stefanou N, Kiyanova A, Efremov M, Fytas G and Nealey P 2007 Elastic properties and glass transition of supported polymer thin films *Macromolecules* **40** 7283–90

[20] Mäthger L M, Denton E J, Marshall N J and Hanlon R T 2009 Mechanisms and behavioural functions of structural coloration in cephalopods *J. R. Soc. Interface* **6** (Suppl 2) S149–63

[21] Parker A R 2000 515 million years of structural colour *J. Opt. A: Pure Appl. Opt.* **2** R15

[22] Rudykh S and Boyce M C 2014 Transforming wave propagation in layered media via instability-induced interfacial wrinkling *Phys. Rev. Lett.* **112** 034301

[23] Li Y, Kaynia N, Rudykh S and Boyce M C 2013 Wrinkling of interfacial layers in stratified composites *Adv. Eng. Mater.* **15** 921–6

[24] Bowden N, Brittain S, Evans A G, Hutchinson J W and Whitesides G M J N 1998 Spontaneous formation of ordered structures in thin films of metals supported on an elastomeric polymer *Nature* **393** 146

[25] Jiang H, Khang D-Y, Song J, Sun Y and Huang Y 2007 Rogers, Finite deformation mechanics in buckled thin films on compliant supports *Proc. Natl Acad. Sci.* **104** 15607–12

[26] Chen C-M, Reed J C and Yang S 2013 Guided wrinkling in swollen, pre-patterned photoresist thin films with a crosslinking gradient *Soft Matter* **9** 11007–13

[27] Schweikart A, Pazos-Pérez N, Alvarez-Puebla R A and Fery A 2011 Controlling inter-nanoparticle coupling by wrinkle-assisted assembly *Soft Matter.* **7** 4093–100

[28] Wang S and Ding T 2018 Buckling polystyrene beads with light *Nanoscale* **10** 16293–7

[29] Ibbotson L A and Baumberg J J 2013 Fabricating large-area metallic woodpile photonic crystals using stacking and rolling *Nanotechnology* **24** 305301

[30] Zaumseil J, Meitl M A, Hsu J W, Acharya B R, Baldwin K W, Loo Y-L and Rogers J A 2003 Three-dimensional and multilayer nanostructures formed by nanotransfer printing *Nano Lett.* **3** 1223–7

[31] Jandron M and Henann D L 2018 A numerical simulation capability for electroelastic wave propagation in dielectric elastomer composites: application to tunable soft phononic crystals *Inter. J. Solids Struct.* **150** 1–21

[32] Baer E, Hiltner A and Keith H 1987 Hierarchical structure in polymeric materials *Science* **235** 1015–22

[33] Liu R Y, Jin Y, Hiltner A and Baer E 2003 Probing nanoscale polymer interactions by forced-assembly *Macromol. Rapid Commun.* **24** 943–8

[34] Lockwood D J and Young J F 2013 *Light Scattering in Semiconductor Structures and Superlattices* vol 273 (Berlin: Springer)

[35] Psarobas I, Papanikolaou N, Stefanou N, Djafari-Rouhani B, Bonello B and Laude V 2010 Enhanced acousto-optic interactions in a one-dimensional phoxonic cavity *Phys. Rev.* B **82** 174303

[36] Riobóo R J J, Sánchez-Sánchez A and Prieto C 2016 Optical find of hypersonic surface acoustic waves in bulk transparent materials *Phys. Rev.* B **94** 014313

[37] Lazarenkova O L and Balandin A A 2003 Raman scattering from three-dimensionally regimented quantum dot superlattices *Superlattices Microstruct.* **33** 95–101

[38] Alonso-Redondo E, Gueddida A, Li J, Graczykowski B, Torres C S, Pennec Y, Yang S, Djafari-Rouhani B and Fytas G 2017 Directional elastic wave propagation in high-aspect-ratio photoresist gratings: liquid infiltration and aging *Nanoscale* **9** 2739–47

[39] Sandercock J 1972 Brillouin-scattering measurements on silicon and germanium *Phys. Rev. Lett.* **28** 237

[40] Groenen J, Poinsotte F, Zwick A, Torres C S, Prunnila M and Ahopelto J 2008 Inelastic light scattering by longitudinal acoustic phonons in thin silicon layers: from membranes to silicon-on-insulator structures *Phys. Rev.* B **77** 045420

[41] Friedman E, Ritger A and Andrews R 1969 Brillouin scattering near the glass transition of polymethyl methacrylate *J. Appl. Phys.* **40** 4243–7

[42] Mitchell R and Guillet J 1974 Brillouin scattering in amorphous polymeric solids *J. Polym. Sci. Polym. Phys. Ed.* **12** 713–33

[43] Kearns K L, Still T, Fytas G and Ediger M 2010 High-modulus organic glasses prepared by physical vapor deposition *Adv. Mater.* **22** 39–42

[44] Cang Y, Reuss A N, Lee J, Yan J, Zhang J, Alonso-Redondo E, Sainidou R, Rembert P, Matyjaszewski K and Bockstaller M R 2017 Thermomechanical properties and glass dynamics of polymer-tethered colloidal particles and films *Macromolecules* **50** 8658–69

[45] Mirigian S and Schweizer K S 2014 Elastically cooperative activated barrier hopping theory of relaxation in viscous fluids: II. Thermal liquids *J. Chem. Phys.* **140** 194507

[46] Galich P I, Fang N X, Boyce M C and Rudykh S 2017 Elastic wave propagation in finitely deformed layered materials *J. Mechan. Phys. Solids* **98** 390–410

[47] Galich P I and Rudykh S 2017 Shear wave propagation and band gaps in finitely deformed dielectric elastomer laminates: long wave estimates and exact solution *J. Appl. Mech.* **84** 091002